AAS 11-131

TRAJECTORY DESIGN USING PERIAPSE POINCARÉ MAPS AND INVARIANT MANIFOLDS

A. F. Haapala* **and K. C. Howell†**

Previous researchers have demonstrated that the periapse Poincaré map is very useful to deliver insight into trajectory behavior near the smaller primary within the context of the restricted three-body problem. In this investigation, periapse maps are employed as a design tool for the construction of both planar and three-dimensional transit trajectories with predetermined characteristics. The design strategies are demonstrated via examples that include transit trajectories, as well as heteroclinic connections. Besides mission design, these techniques are also applied to generate path approximations for several Jupiter family comets.

INTRODUCTION

The planar manifolds associated with the L_1 and L_2 Lyapunov orbits have been previously demonstrated as separatrices within the context of the Circular Restricted Three-Body Problem (CR3BP).[4,5,8,16] Use of a Poincaré map allows the structures associated with these manifolds to be exploited for trajectory design. In this investigation, periapse Poincaré maps[11,14,15] are employed to compute trajectory arcs that possess distinctive behaviors in the vicinity of P_2, and are valuable in the prediction of available solutions for a given system and a specified value of Jacobi constant. The periapse structures associated with the invariant manifolds originating near planar Lyapunov orbits in the CR3BP are examined as a design tool for the construction of planar trajectories, namely, transit trajectories and heteroclinic connections. A corrections algorithm is developed to precisely locate heteroclinic solutions, and the formulation also allows for a continuation process to examine families of orbits. To generate three-dimensional trajectories, a targeting algorithm is employed to locate three-dimensional analogs to the planar trajectories. Observation of the three-dimensional periapse structures proves valuable in predicting the available solutions in the spatial problem. These strategies are developed within the context of the Sun-Saturn system, and are then applied to study cometary trajectories in the Sun-Jupiter system. Path approximations are generated for comets Kushida-Muramatsu[1993] and 147P/Oterma, both of which possess trajectories that transit the Jupiter region.

*Ph.D. Student, School of Aeronautics and Astronautics, Purdue University, Armstrong Hall of Engineering, 701 W. Stadium Ave, West Lafayette, Indiana 47907-2045.

†Hsu Lo Professor of Aeronautical and Astronautical Engineering, School of Aeronautics and Astronautics, Purdue University, Armstrong Hall of Engineering, 701 W. Stadium Ave, West Lafayette, Indiana 47907-2045; Fellow AAS; Associate Fellow AIAA.

CIRCULAR RESTRICTED THREE-BODY PROBLEM

The dynamical model that is assumed for this analysis is consistent with the formulation in the CR3BP, where the motion of a massless particle, P_3, is examined as it moves in the vicinity of two primary bodies, P_1 and P_2. A rotating frame, centered at the system barycenter, B, is defined such that the rotating $\hat{x}$-axis is defined to be directed from the larger primary (P_1) to the smaller (P_2), the $\hat{z}$-axis is parallel to the direction of the angular velocity of the primary system with respect to the inertial frame, and the $\hat{y}$-axis completes the dextral orthonormal triad. The system is non-dimensionalized using the following characteristic quantities: total mass, $m^* = m_1 + m_2$; the distance between the primaries, $\ell^* = R_1 + R_2$; and, characteristic time, $t^* = \sqrt{\frac{\ell^{*3}}{Gm^*}}$. The non-dimensional distances to the primaries are $r_1 = \mu$, $r_2 = 1 - \mu$. The position vectors defined in terms of rotating coordinates are $\bar{r} = x\hat{x} + y\hat{y} + z\hat{z}$, $\bar{r}_{13} = (x - \mu)\hat{x} + y\hat{y} + z\hat{z}$, and $\bar{r}_{23} = (x - 1 + \mu)\hat{x} + y\hat{y} + z\hat{z}$. The first-order vector equation of motion for the CR3BP is written with respect to the rotating frame in non-dimensional variables as follows,

$$\dot{\bar{x}} = \bar{f}(\bar{x}), \tag{1}$$

where

$$\bar{f} = \left[\begin{array}{cccccc} \dot{x}, & \dot{y}, & \dot{z}, & 2\dot{y} + \Omega_x, & -2\dot{x} + \Omega_y, & \Omega_z \end{array} \right]^T. \tag{2}$$

The pseudo-potential, Ω, is defined $\Omega(x, y, z) = \dfrac{1 - \mu}{r_{13}} + \dfrac{\mu}{r_{23}} + \dfrac{1}{2}(x^2 + y^2)$, and the quantities $\Omega_x, \Omega_y, \Omega_z$ represent partial derivatives of Ω with respect to rotating variables. Five libration points exist, and are depicted in fig.(1(a)). The integral of the motion, known as the Jacobi constant, is represented as $C = 2\Omega(x, y, z) - v^2$, where $v = \sqrt{\dot{x}^2 + \dot{y}^2 + \dot{z}^2}$. From the expression for Jacobi constant, the zero-velocity curves (ZVCs) are defined where $2\Omega(x, y, z) - C = 0$. A sample schematic of a ZVC, for values of Jacobi constant such that $C_{L_3} < C < C_{L_2}$, appears in fig.(1(b)). Here, the region surrounding the larger primary is labeled the *interior* region (I), the region in the

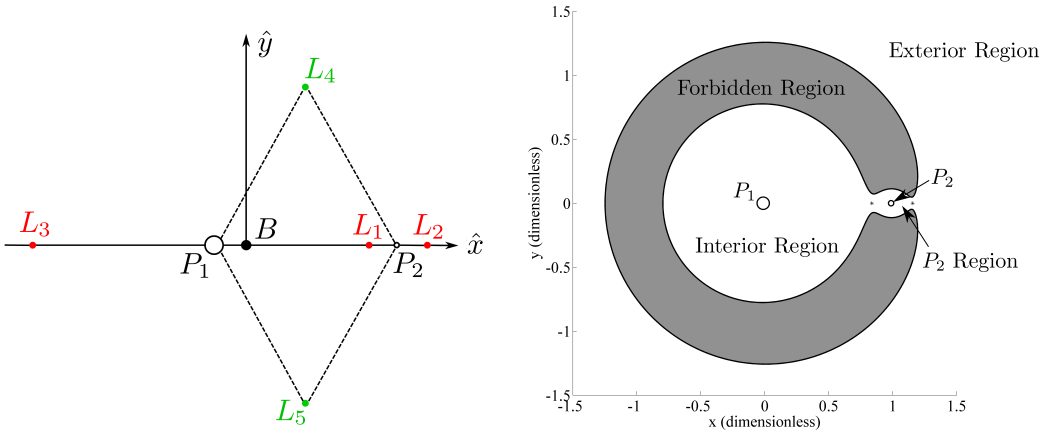

(a) Schematic of libration points

(b) Sample ZVC

Figure 1. Regions of position space delineated by the ZVCs for $C_{L_3} < C < C_{L_2}$. (Earth and Moon at 2x)

vicinity of the smaller primary is defined as the P_2 region (R_{P2}), and the *exterior* region (E) lies

beyond the ZVCs. The mass parameter, μ, as well as the Jacobi constant values associated with the libration points, for various systems appear in Table (1).

Table 1. System Constants

System	μ ($\times 1e{-}4$)	C_{L_1}	C_{L_2}	C_{L_3}	$C_{L_{4/5}}$
Sun-Jupiter	9.538156685350	3.038759285607	3.037487278186	3.000953796543	2.999047094096
Sun-Saturn	2.858042732312	3.017823893248	3.017442768919	3.000285802567	2.999714277411

Invariant Manifolds

For unstable periodic orbits in the CR3BP, higher-dimensional manifold structures exist and prove invaluable in trajectory design. The stable/unstable manifolds are computed by adding a perturbation in the state along a periodic orbit (period T) in the direction of the stable/unstable eigenvector. Assume that $\lambda_s < 1$ and $\lambda_u = 1/\lambda_s$ are the stable and unstable eigenvalues from the monodromy matrix, $\Phi(t_0 + T, t_0)$, corresponding to an unstable periodic orbit in the vicinity of the L_1 and L_2 libration points. Let $\bar{w}_s$ and $\bar{w}_u$ be their associated eigenvectors, computed by solving the equations, $\Phi(t_0+T, t_0)\bar{w}_s = \lambda_s \bar{w}_s$, $\Phi(t_0+T, t_0)\bar{w}_u = \lambda_u \bar{w}_u$. Define $\bar{w}^+$, $\bar{w}^-$ as the two directions associated with each eigenvector. The local half-manifolds, W^{U-}_{loc} and W^{S-}_{loc}, are approximated by introducing a perturbation relative to the fixed point, $\bar{x}^*$, along the periodic orbit in the directions $\bar{w}^-_u$ and $\bar{w}^-_s$, respectively. Likewise, a perturbation relative to $\bar{x}^*$ in the directions $\bar{w}^+_u$ and $\bar{w}^+_s$, respectively, produces the local half-manifolds W^{U+}_{loc} and W^{S+}_{loc}. The step along the direction of the eigenvector is denoted d, and the initial states along the local stable manifolds are as follows,

$$\bar{x}^+_s = \bar{x}^* + d \cdot \bar{w}^+_s, \tag{3}$$

$$\bar{x}^-_s = \bar{x}^* - d \cdot \bar{w}^-_s, \tag{4}$$

where $\bar{w}^+_s$ and $\bar{w}^-_s$ are of unit length. The value of d is critical because it determines the accuracy with which the local manifolds are approximated. The local stable manifolds are globalized by propagating the states $\bar{x}^+_s$ and $\bar{x}^-_s$ in reverse time in the nonlinear model. This process yields the numerical approximation for the global manifolds $W^{S+}_{\bar{x}^*}$ and $W^{S-}_{\bar{x}^*}$, respectively. The same procedure is employed to approximate the unstable global manifolds, $W^{U+}_{\bar{x}^*}$ and $W^{U-}_{\bar{x}^*}$. The collection of the stable and unstable manifolds corresponding to each fixed point along a planar Lyapunov orbit form what are often denoted as the manifold "tubes".

PERIAPSE SURFACE OF SECTION

Within the context of the planar CR3BP (PCR3BP), the use of a Poincaré section, in addition to a constraint on Jacobi constant, yields a reduction to a two-dimensional system. The state space is, therefore, entirely represented by the projection onto a plane. The periapse surface of section, previously demonstrated by Villac and Scheeres[14,15] as well as Paskowitz and Scheeres,[11] can be projected and viewed in position space rather than a mixed velocity-position space. In the spatial CR3BP (SCR3BP), the reductions by constraining Jacobi constant and employing a Poincaré map

yield a four-dimensional system. Thus, the state space is no longer fully defined by a planar projection, however, the periapse surface of section still proves to be a useful tool for the visualization of the dynamics in the SCR3BP. Periapsis and apoapsis relative to P_2 are defined such that the radial velocity, $\dot{r}$, of P_3 relative to P_2 is zero, and are distinguishable by the direction of radial acceleration, i.e., $\ddot{r} \geq 0$ at periapse and $\ddot{r} \leq 0$ at apoapse. As an example, the periapse structures associated with invariant manifold tubes corresponding to the planar Lyapunov orbits and a specified Jacobi constant value appear in fig.(2). The manifolds in fig.(2(a)) are propagated through their first pe-

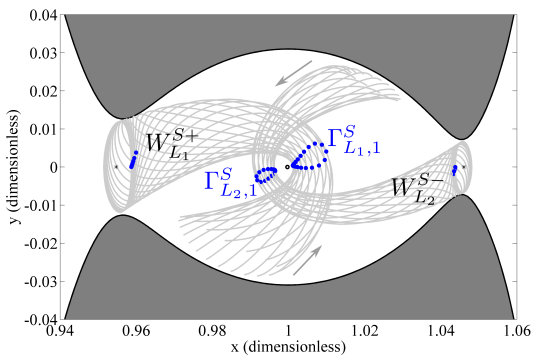

(a) Map of first periapses along of $W^{S+}_{L_1}$ and $W^{S-}_{L_2}$ for $C = 3.0173$ shown in blue.

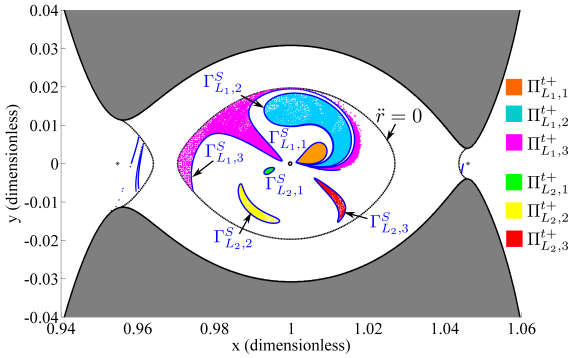

(b) First three periapses along $W^{S+}_{L_1}$, $W^{S-}_{L_2}$, and along L_1 forward-time escapes, and L_2 forward-time escapes for $C = 3.0174$.

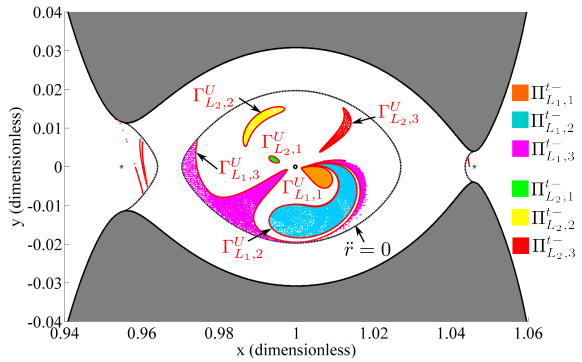

(c) First three periapses along $W^{U+}_{L_1}$, $W^{U-}_{L_2}$, and along L_1 reverse-time escapes, and L_2 reverse-time escapes for $C = 3.0174$.

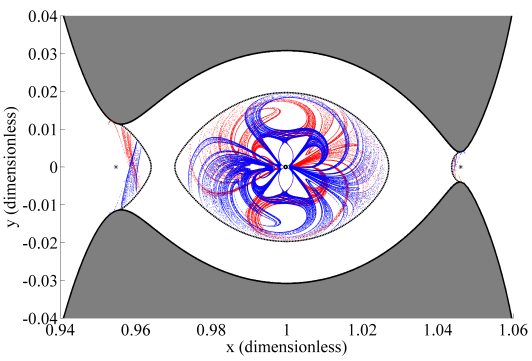

(d) Long-term periapse map associated with $W^{S+}_{L_1}$ (blue) and $W^{U-}_{L_2}$ (red) for $C = 3.0174$.

Figure 2. Manifold periapse structures in the Sun-Saturn system (Saturn at 10x).

riapses, indicated as blue points along the manifold trajectories. Note that, for some trajectories, the first periapsis occurs in the vicinity of the libration point orbit near L_1 or L_2, however these periapses are neglected in this investigation. A map corresponding to the first three periapses along $W^{S+}_{L_1}$ and $W^{S-}_{L_2}$ appears in fig.(2(b)). To examine the evolution of a large number of initial states at this Jacobi level, a batch of escape trajectories is examined by propagating a grid of $\sim 22,000$ apse points within the P_2 region for 212 units in forward time. Those trajectories that cross the boundary $x = x_{L_1} - 0.01$ are defined as forward-time L_1 escape trajectories, while those that cross $x = x_{L_2} + 0.01$ are defined as forward-time L_2 escapes. The colored areas in fig.(2(b)) represent locations of the first three periapses along these L_1 and L_2 forward-time escape trajectories, and are denoted $\Pi^{t+}_{L_1,1\to3}$, and $\Pi^{t+}_{L_2,1\to3}$, respectively, where superscript $t+$ indicates forward-time escape.

The map associated with the first three periapses along the unstable manifolds is simply the reflection of the stable manifold contours from fig.(2(b)) across the $\hat{x}$-axis, as demonstrated in fig.(2(c)). The colored areas in fig.(2(c)) represent locations of the first three periapses along the L_1 and L_2 reverse-time escape trajectories, and are denoted $\Pi^{t-}_{L_1,1\to3}$, and $\Pi^{t-}_{L_2,1\to3}$, respectively, where superscript $t-$ indicates reverse-time escape. Propagating $W^{S+}_{L_1}$ and $W^{U-}_{L_2}$ for a longer interval, i.e., 66 revolutions of the primary system, and plotting the periapses together, the periapse structures appearing in fig.(2(d)) emerge. By previous convention,[5,8] let $\Gamma^{S}_{L_i,m}$ denote the periapse contour formed by the m-th intersection of the stable manifold tube associated with the L_i Lyapunov orbit in the P_2 region, and $\Gamma^{U}_{L_j,n}$ denote the periapse contour formed by the n-th intersection of the unstable manifold tube associated with the L_j Lyapunov orbit in the P_2 region. The delineation between regions of allowed periapsis and apoapsis occurs where $\ddot{r} = 0$, and is plotted as a the dotted black line in figs.(2(b)-2(d)).

APPLICATIONS TO TRAJECTORY DESIGN

Planar Transit Trajectories

Construction of transit trajectories has been previously demonstrated by Koon et al.[8] and Goméz et al.[5] using Poincaré maps corresponding to surfaces of section defined in position space, so that the maps are viewed in a mixed position-velocity space. This investigation employs the periapse surface of section to generate such transit orbits. The Poincaré map associated with the periapse surface can be viewed in configuration space, and therefore provides an intuitive representation of the phase space. Within the context of the PCR3BP, the manifold "tubes" associated with the planar Lyapunov orbits act as separatrices[4,8,6] that distinguish between trajectories that transit between adjoining regions of the ZVCs and those that do not transit. Then, the following propositions apply to a four-dimensional state vector $\bar{x}_0$ along a trajectory, γ, and its subsequent evolution:[6]

1. For $\bar{x}_0$ inside $W^{U+}_{L_1}$, γ, at some time, enters the P_2 region from the interior region through the L_1 gateway in forward time. For $\bar{x}_0$ not inside $W^{U+}_{L_1}$, γ never enters the P_2 region from the interior region in forward time.

2. For $\bar{x}_0$ inside $W^{S+}_{L_1}$, γ, at some time, enters the interior region from the P_2 region through the L_1 gateway in forward time. For $\bar{x}_0$ not inside $W^{S+}_{L_1}$, γ never enters the interior region from the P_2 region in forward time.

3. For $\bar{x}_0$ inside $W^{S-}_{L_2}$, γ, at some time, enters the exterior region from the P_2 region through the L_2 gateway in forward time. For $\bar{x}_0$ not inside $W^{S-}_{L_2}$, γ never enters the exterior region from the P_2 region in forward time.

4. For $\bar{x}_0$ inside $W^{U-}_{L_2}$, γ, at some time, enters the P_2 region from the exterior region through the L_2 gateway in forward time. For $\bar{x}_0$ not inside $W^{U-}_{L_2}$, γ never enters the P_2 region from the exterior region in forward time.

By selecting initial conditions corresponding to periapsis within the region inside both contours $\Gamma^{S}_{L_i,m}$ and $\Gamma^{U}_{L_j,n}$ and propagating in both forward and reverse time, a transit orbit, γ, passing through the L_i- gateway in forward time and the L_j-gateway in reverse time is produced.[5,6,8] Defining one revolution about P_2 as consisting of one periapsis and one apoapsis, γ experiences $p = m+n-3/2$ revolutions about P_2. Thus, to design transit trajectories with some desired behavior in the vicinity

of P_2, the contours $\Gamma^S_{L_i,m}$ and $\Gamma^U_{L_j,n}$ are considered such that $m+n=p+3/2$, where, for an I-to-I transit $i=j=1$, for an E-to-E transit $i=j=2$, for an I-to-E transit $i=2$, $j=1$, and for an E-to-I transit $i=1$, $j=2$. To design E-to-I and I-to-I transit orbits, the map appearing in fig.(2(d)) is employed. Consider, first, the subset of escape trajectories that connect the interior and exterior regions of the ZVCs. In this example, the set of transit trajectories that shifts from the exterior to interior regions is examined. However, the set of transit trajectories that transport in the opposite direction are easily defined via the symmetry properties of the CR3BP. All periapse intersections at this energy level belonging to $W^{S+}_{L_1}$ and $W^{U-}_{L_2}$ are depicted in fig.(2(d)) in blue and red, respectively, as they evolve over approximately 66 revolutions of the primary system. After entering the L_2 gateway, all E-to-I transit trajectories reach their first periapsis within the first contour $\Gamma^U_{L_2,1}$, which is identified in fig.(2(c)). Likewise, the last periapsis before exiting through the L_1 gateway occurs within the first contour $\Gamma^S_{L_1,1}$ from fig.(2(b)). Choosing $n=1$, $m=10$, it is possible to obtain trajectories with a maximum of $p=9.5$ revolutions about P_2, although increasing n, m, or both could certainly yield $p\geq 9.5$. This scenario, ($m=10$, $n=1$), is illustrated in fig.(3). The figure

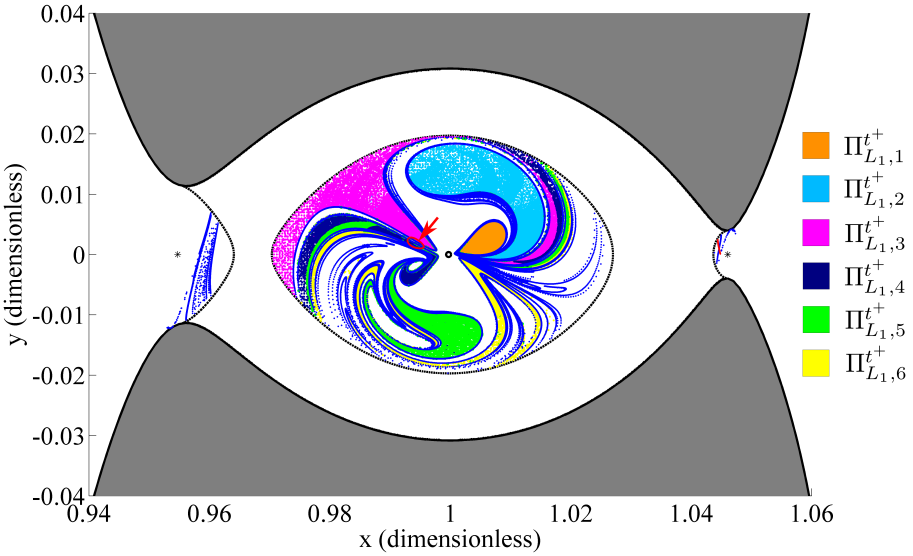

Figure 3. Periapse map employed for locating E-to-I transit trajectories in Sun-Saturn system for $C=3.0174$. Delineation between regions of allowed periapsis and apoapsis appears as dotted black line. (Saturn at 10x)

includes contours $\Gamma^S_{L_1,1\to 10}$, colored in blue, and $\Gamma^U_{L_2,1}$, displayed as a red contour (indicated by the red arrow), and the first six periapses prior to escape through the L_1 gateway appear within the contours as clusters of points, denoted $\Pi^{t+}_{L_1,1\to 6}$, and are plotted in orange, cyan, magenta, navy, green, and yellow, respectively. After arrival from the exterior region through $\Gamma^U_{L_2,1}$, an E-to-I transit trajectory passes through a number $(m+n-1)$ of periapses in the P_2-region and then exits via $\Gamma^S_{L_1,1}$. A close view of contour $\Gamma^U_{L_2,1}$ appears in fig.(4(a)). Clearly, an intersection of contours $\Gamma^U_{L_2,1}$ and $\Gamma^S_{L_1,m}$ does not exist for $m\leq 2$, thus, for this system and value of Jacobi constant, it is predicted that E-to-I (I-to-E) transits corresponding to $p=0.5,\ 1.5$ do not exist. Regions where the interiors of contours $\Gamma^U_{L_2,1}$ and $\Gamma^S_{L_1,3\to 5}$ overlap, yielding $p=2.5$, 3.5, 4.5 transits, are colored in magenta, navy, and green, respectively. Representative samples of E-to-I transit trajectories generated from the periapse initial conditions marked as red points in fig.(4(a)) are also plotted in fig.(4) with initial conditions circled in black. The transit orbits with $p=2.5$, 3.5, 4.5 revolutions about P_2 appear in

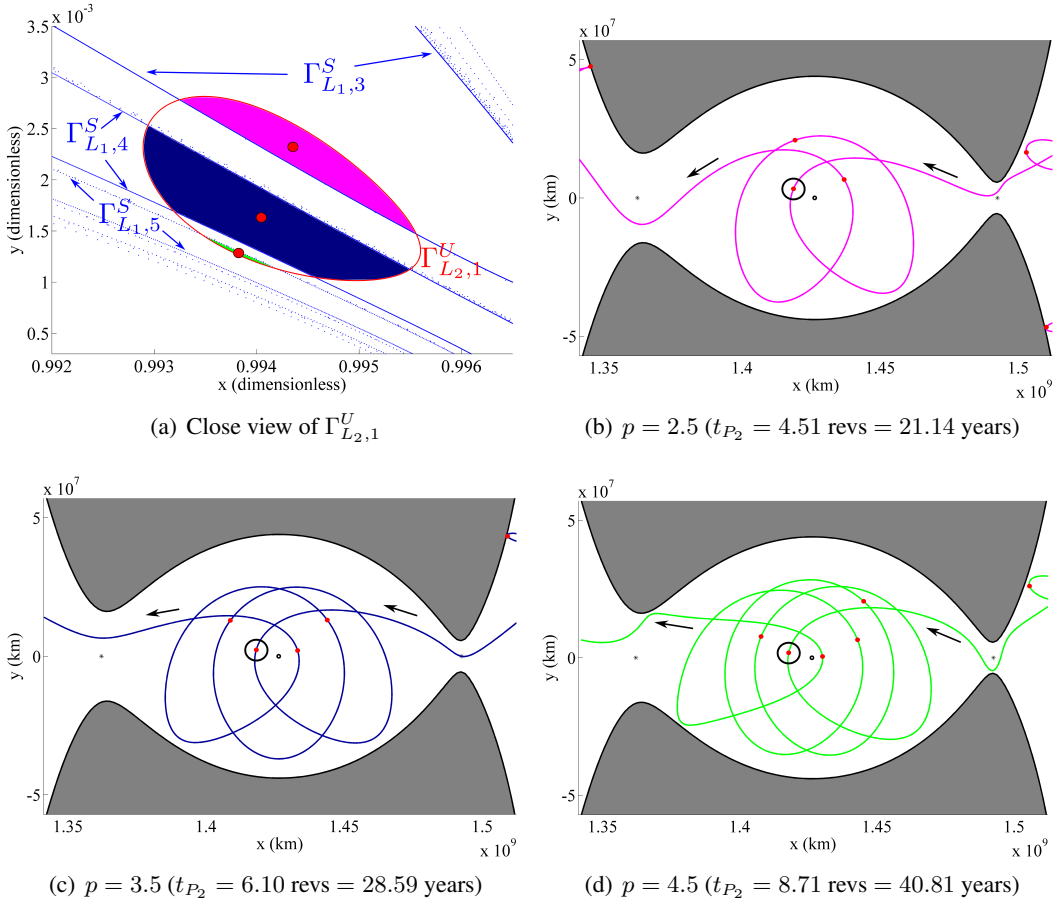

(a) Close view of $\Gamma^U_{L_2,1}$

(b) $p = 2.5$ ($t_{P_2} = 4.51$ revs $= 21.14$ years)

(c) $p = 3.5$ ($t_{P_2} = 6.10$ revs $= 28.59$ years)

(d) $p = 4.5$ ($t_{P_2} = 8.71$ revs $= 40.81$ years)

Figure 4. Transit orbits of varying numbers of revolutions about Saturn appear with periapses in green. ($\ell^* = 1.4267254e^9$ **km)**

figs. (4(b))-(4(d)). The time duration, t_{P_2}, for which each trajectory remains in the vicinity of P_2 is defined as the time required to travel from $x = x_{L_2}$ to $x = x_{L_1}$, and is listed in the caption for each example in terms of both revolutions of the primary system and in years. While only three sample transit trajectories are demonstrated, transit orbits corresponding to $p > 4.5$ revolutions do exist in the Sun-Saturn system at $C = 3.0174$. The transit trajectories in fig.(4) are propagated for 2000 years in the Sun-Saturn system, 1000 years each in forward and reverse time, demonstrating that, for these examples, once escape from P_2 occurs, the trajectory does not return during the propagation time interval.

Heteroclinic Connections

Periapse Poincaré maps can additionally be employed to design heteroclinic connections between Lyapunov orbits. Heteroclinic trajectories in the P_2 region of the ZVCs are located where either $W^{U+}_{L_1} \bigcap W^{S-}_{L_2}$ or $W^{S+}_{L_1} \bigcap W^{U-}_{L_2}$. Let γ be a heteroclinic trajectory possessing a periapsis located in the intersection of contours $\Gamma^S_{L_i,m}$ and $\Gamma^U_{L_j,n}$. The number of revolutions about P_2 that comprises γ is predicted by the expression $p = m + n - 3/2$. This investigation is restricted to include only $i = 1$, $j = 2$, however, arcs evolving in the opposite direction are constructed via the symmetry properties in the CR3BP. If a heteroclinic connection exists, its computation requires the location

of the intersection $\Gamma^U_{L_i,m} \bigcap \Gamma^S_{L_j,n}$. In practice, however, the search for a periapsis in $\Gamma^U_{L_i,m} \bigcap \Gamma^S_{L_j,n}$ yields only an approximation to the heteroclinic orbit. This approximation is used to seed the initial guess for the actual trajectory and a multiple-shooting algorithm is applied to correct the original states. One periapsis along the desired orbit lies within $\Gamma^U_{L_i,m} \bigcap \Gamma^S_{L_j,n}$. Define $\bar{x}_1 \in \Gamma^U_{L_i,m}$ and $\bar{x}_2 \in \Gamma^S_{L_j,n}$ as the nearest points to $\Gamma^U_{L_i,m} \bigcap \Gamma^S_{L_j,n}$. Propagating the state $\bar{x}_1$ in reverse time produces a trajectory, γ_1, that is an unstable manifold trajectory associated with the L_i Lyapunov orbit and, therefore, asymptotically approaches the L_i Lyapunov orbit. Likewise, propagating the state $\bar{x}_2$ in forward time produces a trajectory, γ_2, that corresponds to a stable manifold of the L_j Lyapunov orbit, thus, asymptotically approaching the L_j Lyapunov orbit. The initial guess to represent the orbit is generated by concatenating these asymptotic trajectories to form $\gamma = \{\gamma_1 \bigcup \gamma_2\}$, where γ contains a single point of discontinuity. Let $\bar{x}^*$ represent a fixed point along a Lyapunov orbit of period P, where $\bar{x}^*(0) = \bar{x}^*(P)$ is the location along the orbit where $y = 0$, $\dot{y} > 0$. Let τ represent a coast time along the Lyapunov orbit, i.e., some fraction of the Lyapunov orbital period, so that $\bar{x}^*(\tau = \frac{1}{2}P)$ represents the location along the Lyapunov orbit where $y = 0$, $\dot{y} < 0$. Finally, let t represent the time-of-flight along a manifold. Then, the unstable (stable) manifold arc may be defined via the departure location $\bar{x}^*(\tau_u)$ ($\bar{x}^*(\tau_s)$) along the Lyapunov orbit, and the manifold coast time t_u (t_s). Varying the parameters τ_u, τ_s, and either t_u or t_s, it is possible to iteratively update the trajectory and remove the discontinuity within γ. Because the Jacobi constant along each of the manifold arcs is equal to that of the Lyapunov orbit, it is necessary only to enforce continuity in three of four planar state space variables. Define the initial state along the unstable manifold consistent with eq.(3 or 4), and the final state along the unstable manifold as $\bar{x}_{uf} = \bar{x}_u(t_u)$. The partial derivatives of $\bar{x}_{uf}$ with respect to parameters τ_u, t_u are as follows,[12]

$$\frac{\partial \bar{x}_{uf}}{\partial t_u} = \dot{\bar{x}}_{uf}, \tag{5}$$

$$\frac{\partial \bar{x}_{uf}}{\partial \tau_u} = \Phi(t_u, 0) \left[\dot{\bar{x}}^*(\tau_u) + d \left[I_6 - \bar{w}_u(\tau_u) \bar{w}_u(\tau_u)^T \right] A(\bar{x}^*(\tau_u)) \bar{w}_u(\tau_u) \right], \tag{6}$$

where $\bar{w}_u(\tau_u)$ denotes the eigenvector ($\bar{w}_u^+$ or $\bar{w}_u^-$) associated with the fixed point $\bar{x}^*(\tau_u)$ along the L_2 Lyapunov orbit. Of course, eqs.(5-6) are also derived for the stable manifold. A constraint function, $\bar{F}$, and a vector, $\bar{Q}$, of design variables are defined such that $\bar{F}(\bar{Q}^*) = \bar{0}$ for the desired solution $\bar{Q}^*$. Using a first-order Taylor expansion, $\bar{F}(\bar{Q}^*) = \bar{F}(\bar{Q}) + D\bar{F} \cdot (\bar{Q}^* - \bar{Q})$, where

$$\bar{Q} = \left[\begin{array}{ccc} \tau_u & \tau_s & t_s \end{array} \right]^T, \tag{7}$$

$$\bar{F}(\bar{Q}) = \left[\begin{array}{ccc} x_{sf} - x_{uf}, & y_{sf} - y_{uf}, & \dot{x}_{sf} - \dot{x}_{uf} \end{array} \right]^T, \tag{8}$$

$$\tag{9}$$

Defining $\delta\bar{Q} = \bar{Q}^* - \bar{Q}$, the design variables are updated by adding the perturbation

$$\delta\bar{Q} = -D\bar{F}^{-1}\bar{F}(\bar{Q}). \tag{10}$$

Thus, the parameters τ_u, τ_s, and t_u (t_s) are varied until $\|\bar{F}\| < \epsilon$, where ϵ represents the selected tolerance for convergence. Because the system is nonlinear, multiple updates may be required to reach a solution $\bar{Q}^*$ such that $\|\bar{F}(\bar{Q}^*)\| = 0$ to within the desired tolerance. Due to system sensitivities, it may be necessary to include additional patch points, or nodes, along each manifold to distribute the sensitivities and to achieve convergence to an acceptable tolerance.[1,2,6,13]

Consider, now, heteroclinic trajectories connecting the L_1 and L_2 Lyapunov orbits. A close view of the contours $\Gamma^U_{L_2,1} \bigcap \Gamma^S_{L_1,3\to5}$ is illustrated in fig.(5(a)). The locations of periapses corresponding

to heteroclinic connections with $p = 2.5$, 3.5, and 4.5 revolutions about P_2 are represented by magenta, blue, and green markers, respectively. Using the previous procedure, initial guesses are

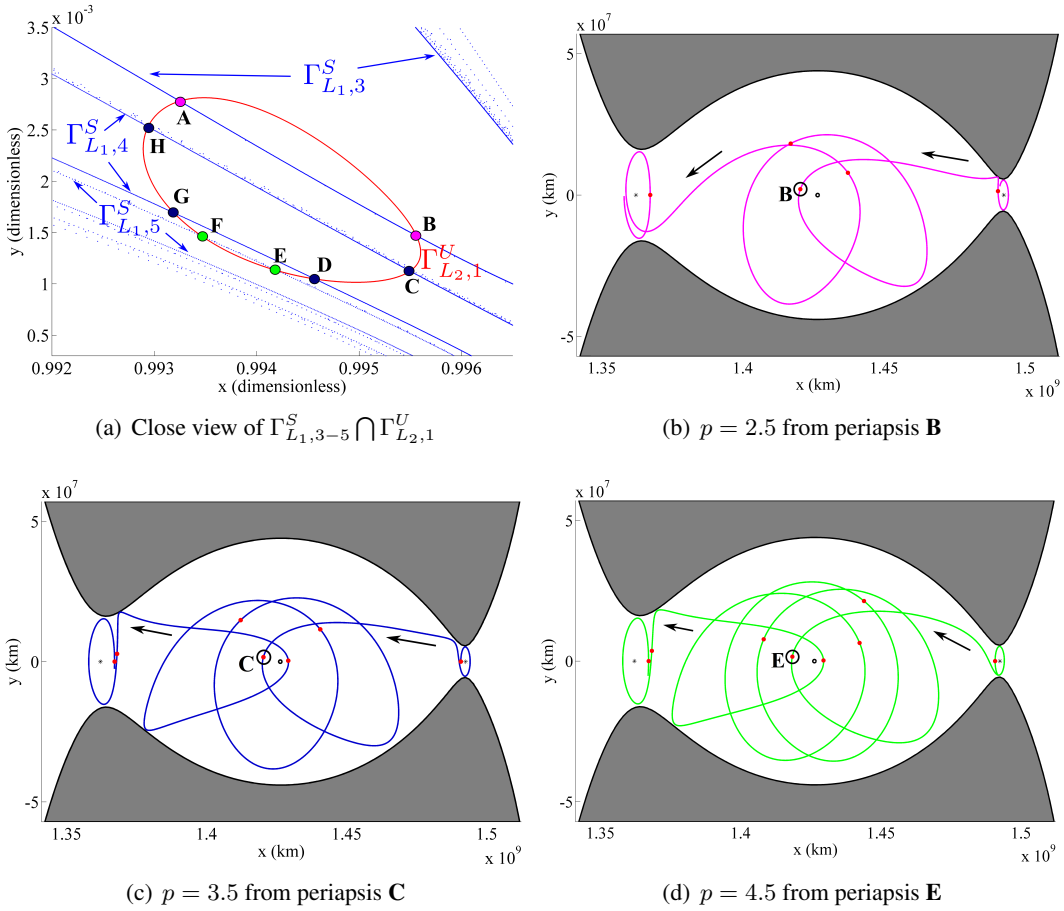

(a) Close view of $\Gamma^S_{L_1,3-5} \bigcap \Gamma^U_{L_2,1}$

(b) $p = 2.5$ from periapsis **B**

(c) $p = 3.5$ from periapsis **C**

(d) $p = 4.5$ from periapsis **E**

Figure 5. Heteroclinic connections incorporating 2.5, 3.5, and 4.5 revolutions about P_2. (Saturn at 10x, $\ell^* = 1.4267254e^9$ km)

obtained from periapses nearby these intersections and are corrected using multiple shooting. Note that, for p =2.5 and 4.5 revolutions, there exist two, and for $p = 3.5$ revolutions there exist four distinct heteroclinic connections. Examples of corrected trajectories, continuous in both position and velocity, are displayed in figs. (5(b))-(5(d)), and the associated parameters appear in Table (2).

Defining each heteroclinic connection in terms of the parameters τ_s, τ_u, $|t_s| + t_u$, it is possible to generate a family of heteroclinic connections using a continuation method. As an example, consider the $p = 2.5$ heteroclinic connection corresponding to periapsis **A** in fig.(5(a)) that appears far left in fig.(6). Stepping down in Jacobi value, corresponding to an increase in energy level, a family of heteroclinic connections is developed in the Sun-Saturn system, without the need to produce multiple Poincaré maps. Examples from the resulting family appear as the center and right subplots in fig.(6), corresponding to Jacobi values $C = 3.016$ and $C = 3.012$, respectively. By increasing the Jacobi constant value, the terminal member of the family of $p = 2.5$ revolution heteroclinic connections is ultimately discovered at approximately $C = 3.01743$, and appears in fig.(7). The Poincaré map corresponding to this Jacobi value appears in fig.(7(b)). It is apparent from this map

Table 2. Parameters Representing a Family of Heteroclinic Connections

Periapsis	τ_s	τ_u	$\lvert t_s \rvert + t_u$
B	-0.011221348055	1.881835081616	11.664087888057
C	-1.398002348626	1.520087768587	13.431256615115
E	-1.315508996003	0.906122925048	15.130165415215

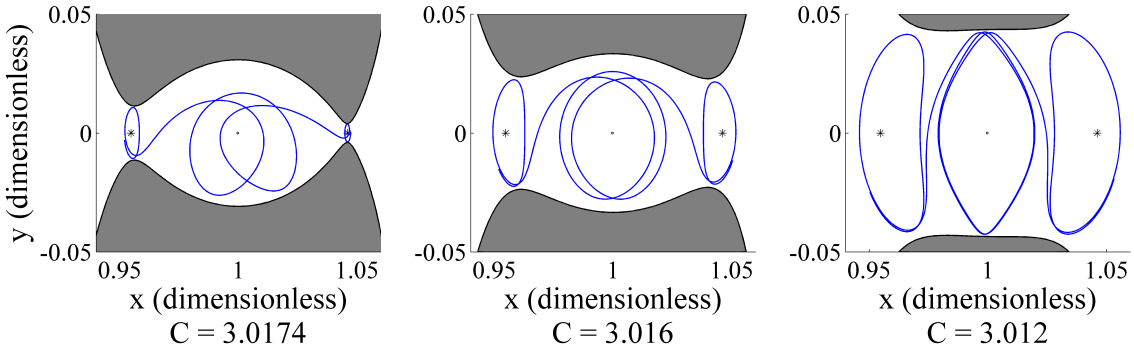

Figure 6. Generating family of heteroclinic solutions, initialized from periapsis A, in the Sun-Saturn system using continuation. (Saturn at 10x)

that $\Gamma^S_{L_1,3} \bigcap \Gamma^U_{L_2,1}$ exists as a single point, signifying that periapses **A,B** have merged. For lower energy levels, $\Gamma^S_{L_1,3} \bigcap \Gamma^U_{L_2,1}$ no longer exists, indicating that the $p = 2.5$ family of heteroclinic connections indeed terminates for approximately this value of Jacobi constant. It is also apparent from fig.(7(b)), that contours $\Gamma^S_{L_1,5}$ and $\Gamma^U_{L_2,1}$ no longer intersect, and therefore no $p = 4.5$ heteroclinic orbits exist for this energy.

Three-dimensional Transit Trajectories

In the SCR3BP, the dimension of the problem is increased and new challenges arise from the perspective of mission design. In the SCR3BP, the invariant manifold tubes no longer behave as separatrices. Additionally, if there exist no known three-dimensional periodic orbits for a particular value of Jacobi constant, manifold trajectories may not be readily available. For these reasons, the process to locate trajectories with specific behaviors is modified from the process employed in the planar problem. The search for forward-time escape trajectories in three-dimensions is simplified if the set of initial conditions is selected such that escape is likely. The following procedure is modified from a process employed by Paskowitz and Scheeres.[11] Initial conditions are selected such that $x(0) = x_{L_i}$ for each point, where i =1 or 2, and $\dot{x}(0)$ is directed away from P_2. A grid of positions in the $y - z$ plane is produced, and the speed relative to the rotating frame for each initial location is generated using the expression for Jacobi constant. For each grid point, there are infinitely many combinations of initial velocities $\dot{x}(0)$, $\dot{y}(0)$, $\dot{z}(0)$ that satisfy $v = (\dot{x}(0)^2 + \dot{y}(0)^2 + \dot{z}(0)^2)^{\frac{1}{2}}$. For completeness, the velocity components are varied for each grid point. First, $|\dot{x}(0)|$ is varied within the range $[0,\, v]$. Then, for each set $(x(0), y(0), z(0), \dot{x}(0))$, the magnitude corresponding to the remaining velocity components that are required to satisfy the Jacobi constant restraint is

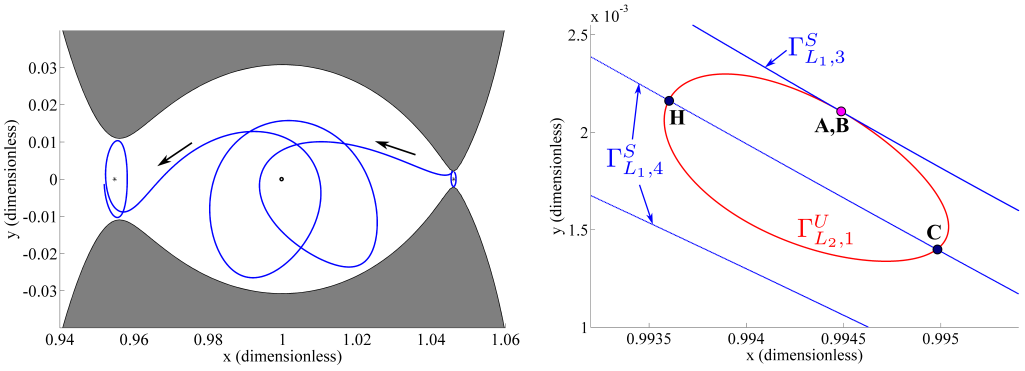

(a) Terminal member of heteroclinic family

(b) Periapse map associated with approximate value of terminal Jacobi constant

Figure 7. Approximate terminal member of a family of heteroclinic solutions in the Sun-Saturn system ($\sim C = 3.01743$). (Saturn at 10x)

$v_{yz} = \sqrt{v^2 - \dot{x}_0^2}$. Define an angle parameter β, which is varied over the interval $0 \leq \beta \leq 2\pi$, and defines individual velocity components such that $\dot{y}(0) = v_{yz}\cos(\beta)$ and $\dot{z}(0) = v_{yz}\sin(\beta)$. Thus, for each point in the grid, the velocity is sampled from a half-sphere of radius v. Three-dimensional reverse-time escape trajectories are easily defined by employing the symmetry properties of the CR3BP.

Defining the grid of initial conditions as detailed, and propagating the initial states in reverse time, it is possible to examine, in three-dimensional space, the resulting sequence of periapse positions that correspond to trajectories that escape from the P_2 region. To ensure that each initial condition corresponds to an escape from the P_2 region for the appropriate set of ZVCs, the initial conditions are first propagated forward in time to check for escape, and those that do not depart from the region are discarded from the set of three-dimensional escapes. The clusters of points, $\Pi^{t^-}_{L_1,1}$ and $\Pi^{t^-}_{L_2,1}$, that represent the first periapses along three-dimensional L_1 and L_2 reverse-time escape trajectories, respectively, are displayed in green in fig.(8), and the contours $\Gamma^U_{L_1,1}$ and $\Gamma^U_{L_2,1}$ are plotted in red for reference. The clusters, $\Pi^{t^+}_{L_1,1}$ and $\Pi^{t^+}_{L_2,1}$, associated with forward-time escape would appear as the reflection of clusters $\Pi^{t^-}_{L_1,1}$ and $\Pi^{t^-}_{L_2,1}$ across the $\hat{x}$-axis. To produce a three-dimensional analog to fig.(3), the L_1 forward-time escape trajectories are propagated through six periapse passages, and the plot in fig.(9) emerges. The first six periapse clusters $\Pi^{t^+}_{L_1,1-6}$ are depicted, in addition to the reverse-time cluster $\Pi^{t^-}_{L_2,1}$. The L_1 stable manifold periapse contours $\Gamma^S_{L_1,1\to10}$, as well as the unstable manifold contour $\Gamma^U_{L_2,1}$ are included for reference.

To generate three-dimensional transit trajectories, an algorithm designed to target a specific z-amplitude at periapsis, is employed. A three-dimensional periapse state appears in fig.(10). The algorithm is initialized using a planar trajectory, with a specified itinerary, for the initial guess. Because the P_2 region represents a highly sensitive regime, the planar trajectory is segmented into multiple trajectory arcs, using intermediate patch points, to distribute the system sensitivities. To enforce constraints at periapsis, it is necessary to include any periapses of interest as patch points along the trajectory. Assume that the six-dimensional patch point states are corrected during the iteration process. Thus, define the design variable vector to include the initial states, $\bar{x}_{i0} = \bar{x}_i(t_{i0})$,

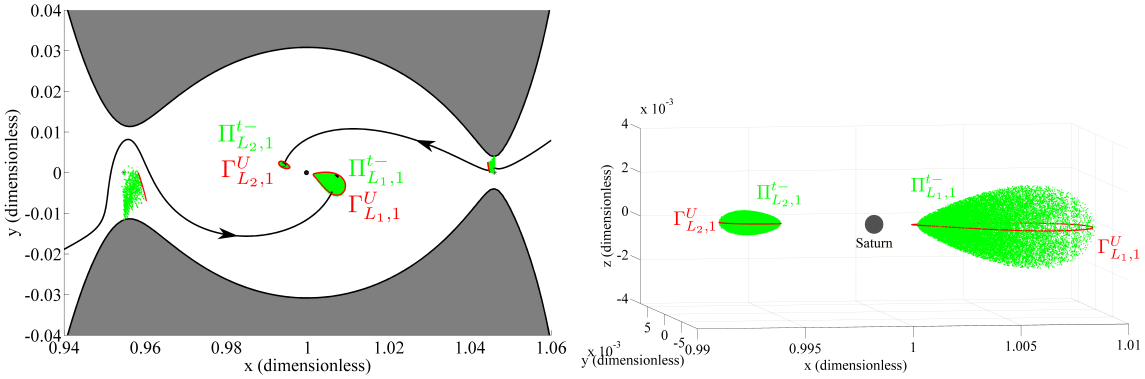

(a) L_1 and L_2 three-dimensional immediate escape periapse cluster projected onto planar configuration space.

(b) Three-dimensional projection of L_1 and L_2 immediate escape periapse clusters.

Figure 8. Three-dimensional reverse-time L_1 and L_2 escape trajectory periapses are projected into configuration space and displayed in green. (Saturn at 10x)

along each trajectory arc, i.e.,

$$\bar{\tilde{Q}} = \left[\; \bar{x}_{10}, \quad \bar{x}_{20}, \quad \ldots, \quad \bar{x}_{n-10}, \quad \bar{x}_{n0} \; \right]^T . \tag{11}$$

Define $\bar{x}_{j0} = [x_p,\ y_p,\ z_p,\ \dot{x}_p,\ \dot{y}_p,\ \dot{z}_p]^T$ as one of the periapsis points along the trajectory, with radius $\rho_p = \left((x_p - 1 + \mu)^2 + y_p^2 + z_p^2\right)^{\frac{1}{2}}$, and velocity $v_p = (\dot{x}_p^2 + \dot{y}_p^2 + \dot{z}_p^2)^{\frac{1}{2}}$ in the rotating frame. The full state $\bar{x}_{j0}$ can be located using the variables ρ_p, θ, ϕ, ψ, as defined in fig.(10), where $\theta = \arctan\left(y_p/(x_p - 1 + \mu)\right)$, $\phi = \arccos\left(z_p/\rho_p\right)$, and $\psi = \arccos\left(\dfrac{\cos(\phi)(\dot{x}_p\cos(\theta) + \dot{y}_p\sin(\theta)) - \dot{z}_p\sin(\phi)}{v_p}\right)$. Note that $\phi > 90^\circ$ when $z_p < 0$, $\psi > 180^\circ$ when $\dot{z}_p > 0$, and $\phi = 90^\circ$ and $\psi = \pm 90^\circ$ for the planar initial guess. These coordinate variables are constrained using the following function,

$$\bar{g} = \left[\; (x_p - 1 + \mu)\dot{x}_p + y_p\dot{y}_p + z_p\dot{z}_p, \quad \rho_p - \rho_p^*, \quad \theta - \theta^*, \quad \phi - \phi^*, \quad \psi - \psi^* \; \right]^T , \tag{12}$$

where $\bar{g} = \bar{0}$ if the constraints are perfectly satisfied. The first element of $\bar{g}$ is necessary to define the patch point as an apse throughout the corrections process because the full state $\bar{x}_{j0}$ is allowed to vary in $\bar{\tilde{Q}}$; then ρ_p^*, θ^*, ϕ^*, ψ^* represent the desired values of ρ_p, θ, ϕ, ψ. Defining the inertial coordinate axes as aligned with the rotating coordinate axes at periapsis, the instantaneous orbital elements ω (argument of periapsis), i (inclination), and Ω (right ascension of the ascending node) can be related to variables ρ_p, v_p, θ, ϕ, ψ as follows: $\omega = \arctan\left(\dfrac{-\cos(\phi)}{\sin(\phi)\cos(\psi)}\right)$, $i = \arcsin\left(\dfrac{\cos(\phi)}{\sin(\omega)}\right)$, and $\Omega = \arctan\left(\dfrac{v_p\sin(\theta)\cos(\psi) + \cos(\theta)\cos(\phi)(v_p\sin(\psi) + \rho_p\sin(\phi))}{v_p\cos(\theta)\cos(\psi) - \sin(\theta)\cos(\phi)(v_p\sin(\psi) + \rho_p\sin(\phi))}\right)$. Of course, true anomaly will be zero at periapsis ($TA = 0$). Thus, a desired three-dimensional periapse state can be targeted in terms of the instantaneous orbital elements at periapsis by applying the constraint

$$\bar{\tilde{g}} = \left[\; (x_p - 1 + \mu)\dot{x}_p + y_p\dot{y}_p + z_p\dot{z}_p, \quad \rho_p - \rho_p^*, \quad \omega - \omega^*, \quad i - i^*, \quad \Omega - \Omega^* \; \right]^T , \tag{13}$$

where ω^*, i^*, Ω^* represent the desired instantaneous orbital elements at the periapsis of interest. Because $Omega$ and $omega$ are undefined in the planar case, constraint function $\bar{g}$ is used to initialize

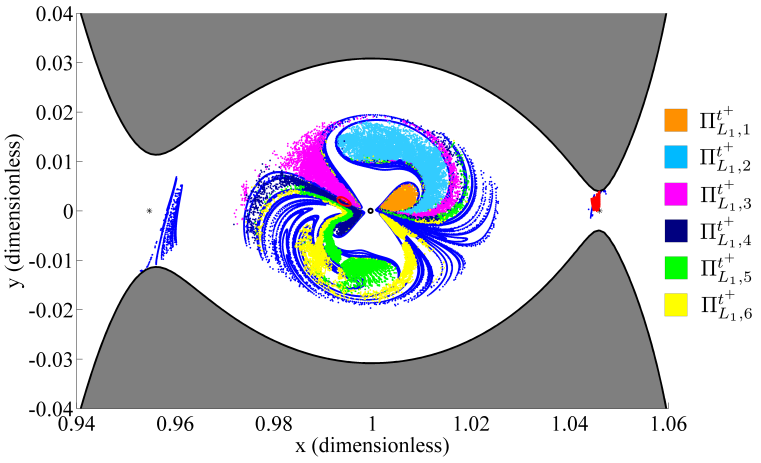

(a) Planar view

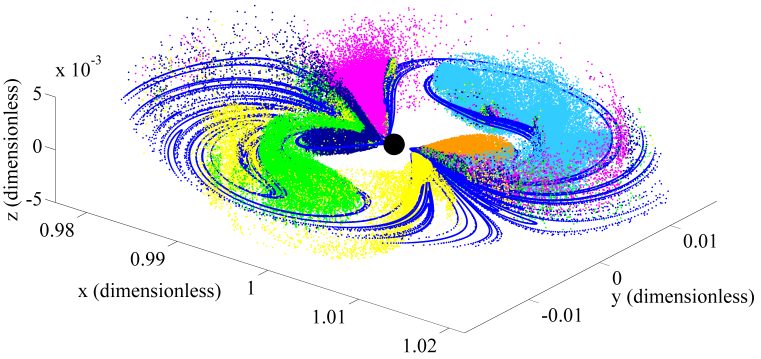

(b) Three-dimensional view

Figure 9. Three-dimensional periapse structures employed to locate three-dimensional E-to-I transits in the Sun-Saturn system for $C = 3.0174$. (Saturn at 10x)

the transition from planar to three-dimensional trajectories. To enforce that the final converged trajectory is continuous, satisfies the periapsis constraints, and maintains the desired value of Jacobi constant, C^*, throughout the corrections process, the following constraint function, $\tilde{\bar{F}}$, is employed:

$$\tilde{\bar{F}} = \left[\; \bar{x}_{20} - \bar{x}_{1f}, \quad \bar{x}_{30} - \bar{x}_{2f}, \quad \ldots, \quad \bar{x}_{n0} - \bar{x}_{n-1f}, \quad \bar{G}^T, \quad C_{10} - C^* \; \right]^T, \tag{14}$$

where $\bar{x}_{if} = \bar{x}_i(t_{if})$ represents the final state along the i-th trajectory segment and $\bar{G}$ represents either $\bar{g}$ or $\tilde{\bar{g}}$, as desired. The vector $\tilde{\bar{Q}}$ is iteratively updated using eq.(10) until $\|\tilde{\bar{F}}(\tilde{\bar{Q}})\| = 0$ to the desired tolerance. Possible values for ρ_p, ϕ, θ are obtained by inspecting the three-dimensional periapse structures in figs.(8,9). For example, the first periapsis in the P_2 region along a three-dimensional, $p = 2.5$ revolution E-to-I trajectory occurs both within the green cluster, $\Pi^{t-}_{L_2,1}$, on the left in fig.(8) and within the magenta cluster, $\Pi^{t+}_{L_1,3}$, in fig.(9). Therefore, the range of values for ρ_p, ϕ, θ must be within those defined by the periapse structures in these figures. A sample set of $p = 2.5$ E-to-I transits is generated for $\omega = 115°$, $\rho_p = 0.006$, $\Omega = 42.5°$ (magenta) and $\omega = 295°$, $\rho_p = 0.006$, $\Omega = 222.5°$, (blue) and for the range $i = 1, 2, 3, 4, 4.7°$, and is plotted in fig.(11). Note that the blue trajectories are simply the reflection of the magenta trajectories across the $x - y$ plane.

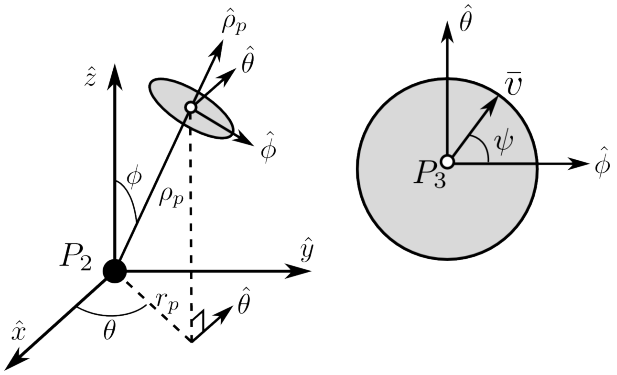

Figure 10. Three-dimensional periapsis state.

For $i > 4.7°$, the targeting algorithm does not converge on a $p = 2.5$ E-to-I transit, indicating that the maximal inclination for the first periapsis along an E-to-I transit occurs around $i = 4.7°$. To verify this, a close view of the locations of the first periapses appear as red dots in fig.(12) along with the first periapse cluster $\Pi^{t-}_{L_2,1}$. Clearly, when $i = 4.7°$, periapsis lies on the surface of this cluster. As in the planar case, these techniques can be extended to generate three-dimensional

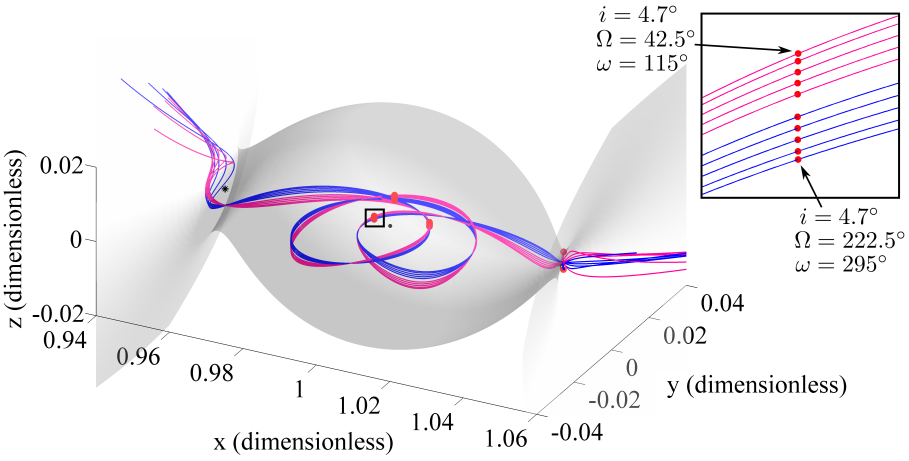

Figure 11. Examples of three-dimensional E-to-I transits in the Sun-Saturn system for $1° \leq i \leq 4.7°$, $\rho_p = 0.006$, $z_p > 0$: ($\omega = 115°$, $\Omega = 42.5°$), $z_p > 0$: ($\omega = 295°$, $\Omega = 222.5°$), $C = 3.0174$. (Saturn at 10x)

trajectories possessing varying numbers of revolutions about P_2, and could additionally be used to locate three-dimensional I-to-I and E-to-E transits.

APPLICATIONS TO COMETARY TRAJECTORIES

Using the previously demonstrated techniques, both I-to-I and E-to-E transits are designed by considering the appropriate manifolds. In addition, these techniques are successfully applied to other systems with different values of the relative mass parameter, μ. The Sun-Jupiter system possesses many naturally occurring examples of trajectories in the vicinity of P_2 in the form of cometary paths.[3] Many Jupiter family comets are temporarily captured in the vicinity of Jupiter, thereby experiencing at least one periapsis near the planet. As an example, the naturally occuring

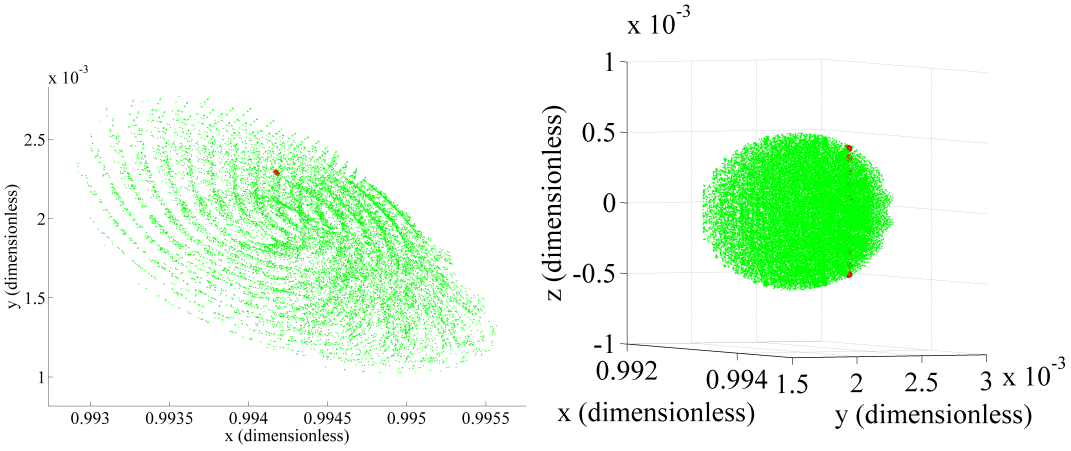

(a) planar view (b) $3-D$ view

Figure 12. Close view of cluster $\Pi^{t-}_{L_2,1}$ (green), with three-dimensional E-to-I periapses (red); the periapses with maximum inclination lie on the surface of the cluster.

path of comet 147P/Kushida-Muramatsu[1993] (K-M1993)[10] is classified as an I-to-I transit, which, between 1949 and 1961, enters the Jupiter region from the interior region, experiences $p = 2.5$ revolutions about Jupiter, and returns to the interior region of the ZVCs. To approximate the cometary path, the PCR3BP is the model assumed, in addition to a Jacobi constant value of $C = 3.02$. For this high energy level, the periapse contours appear significantly different from those in fig.(3). Return momentarily to the Sun-Saturn system for illustration. Considering fig.(13), where periapse contours $\Gamma^S_{L_1,1}$ (left) and $\Gamma^S_{L_2,1}$ (right) are displayed for four energies in the Sun-Saturn system, it is apparent that, as energy increases, these contours increase in size. The ZVCs for the four energies are also included in the figure, where the lowest value of Jacobi constant corresponds to the most open ZVC in the vicinity of P_2. For the largest energy displayed, the contours extend beyond the boundary of allowed periapses, thus the contours are no longer closed, as demonstrated in fig.(13(b)). Applying this information to the Sun-Jupiter system, the manifold periapse contours

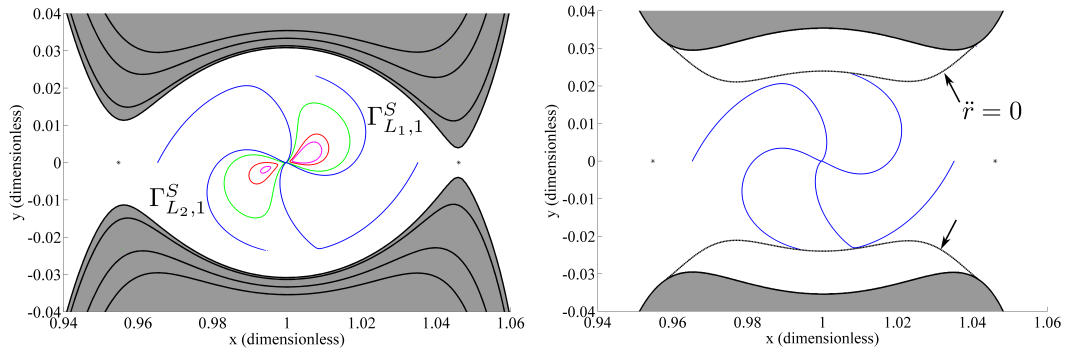

(a) $\Gamma^S_{L_1,1}$ and $\Gamma^S_{L_2,1}$ are demonstrated for $C = 3.0174$ (magenta), $C = 3.0171$ (red), $C = 3.016$ (green), and $C = 3.015$ (blue)

(b) $\Gamma^S_{L_1,1}$ and $\Gamma^S_{L_2,1}$ appear with the boundary of allowed periapsis for $C = 3.015$

Figure 13. Regions of escape periapse for varying Jacobi constant values in the Sun-Saturn system.

$\Gamma^U_{L_1,n}$ and $\Gamma^S_{L_1,m}$ are considered for the approximation of the path of K-M1993, such that $n+m=4$. These contours appear in fig.(14(a)), with the thin region that lies inside both contours $\Gamma^U_{L_1,1}$ and $\Gamma^S_{L_1,3}$ colored in cyan, as well as the black dotted contour (indicated with arrows) distinguishing regions of periapse and apoapse. The periapsis of K-M1993 that lies within $\Gamma^U_{L_1,1} \bigcap \Gamma^S_{L_1,3}$ appears in red, while the periapsis of the approximated trajectory is plotted in green. The resulting planar approximation for the cometary path appears in blue in fig.(14(b)) and requires a duration of about

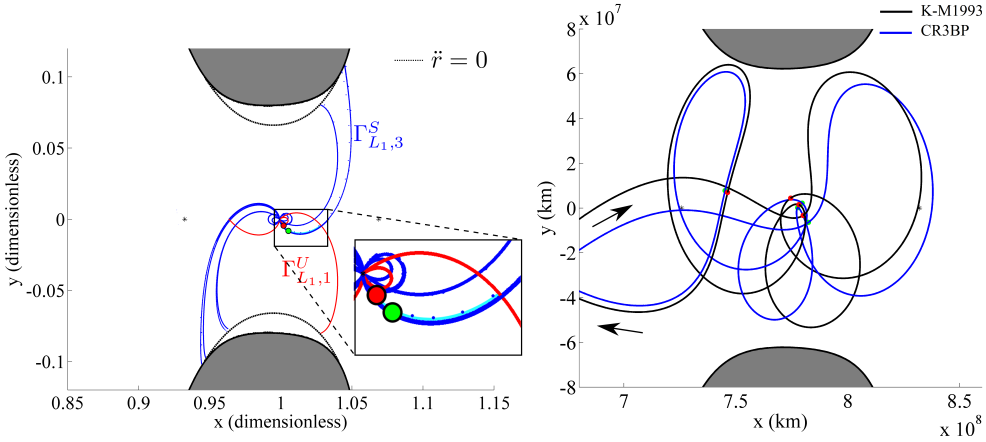

(a) Periapse map demonstrating region of intersection (cyan) of $\Gamma^U_{L_1,1}$ and $\Gamma^S_{L_1,3}$

(b) Comet K-M1993 between 1928 and 1943

Figure 14. Approximating the path of comet K-M1993 in the Sun-Jupiter system for $C=3.02$. ($\ell^* = 7.7841202e^8$ km)

$t = 14.63$ years, which compares closely to the 14.93 year time period observed for the comet. Of course, the true path of K-M1993 is three-dimensional, and possesses a maximum z-amplitude of $0.01420 = 1.106 \times 10^7$ km during the observed time. The planar projection of the cometary path is plotted in fig.(14(b)) in black. Additional cometary path approximations generated using this method are demonstrated by Haapala.[6]

Long-Term Transit Trajectories

The previous examples demonstrate the use of the periapse Poincaré map to generate transit trajectories possessing short-term behaviors, however, these techniques can be extended to produce trajectories with longer itineraries, as previously demonstrated by Koon et al.[8] as well as Goméz et al.[5] One example of a naturally occuring transit trajectory with a long-term itinerary is the path of comet 39P/Oterma between 1910 and 1980, appearing in figure (15). During this time interval, Oterma experiences two encounters with Jupiter, transitioning from the exterior region to the interior during the first encounter, and returning back to the exterior after the second encounter. By employing the periapse Poincaré map, and again assuming the comet exists within the context of the PCR3BP, the long-term behavior for comet Oterma is modeled. (The path of Oterma has been previously approximated by Koon et al.[8] using planar Lyapunov manifolds as well as by Marchand and others[7,9] using three-dimensional halo orbit manifolds.) To generate a path approximation, periapses relative to Jupiter are considered while Oterma is in the P_2 region, and periapses relative to the Sun are considered in the interior region. Points that distinguish perijove appear in fig.(15) as red dots, and points corresponding to perihelion are plotted in green. The periapse maps employed

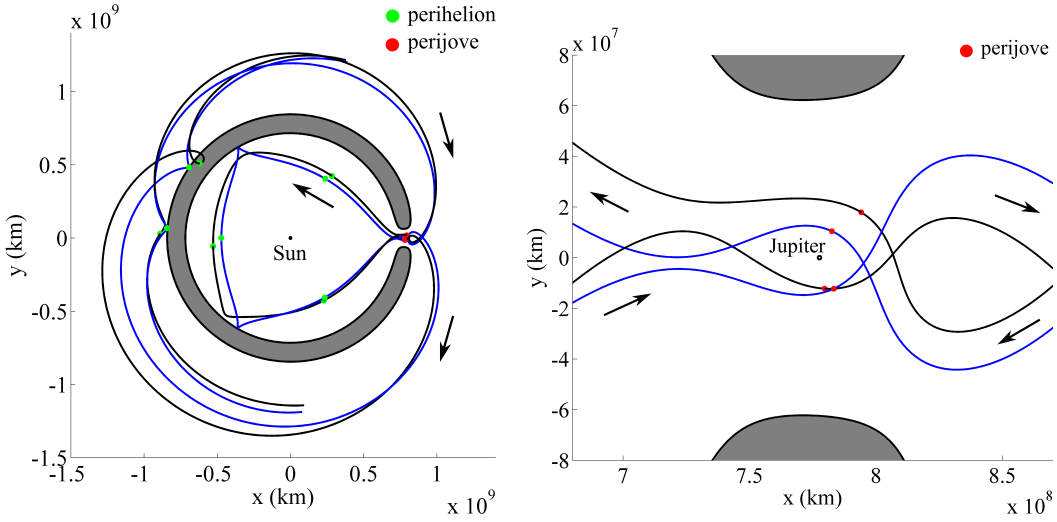

(a) View within Sun-Jupiter rotating frame

(b) Close view of Jupiter region

Figure 15. Path of Oterma between 1910 and 1990 (black) and approximate trajectory in CR3BP (blue). (Sun and Jupiter at 10x , $\ell^* = 7.7841202e^8$ km)

appear in fig.(16). To generate the path approximation, it is convenient to begin with the interior segment of the trajectory, during which Oterma undergoes three perihelion passages. To model this behavior, trajectories along the L_1 Lyapunov orbit manifolds are propagated into the interior region through their first two periapses, generating the perihelion Poincaré map that appears in fig.(16(a)). Selecting perihelion within both contours $\Gamma^{S-}_{L_1,2}$ and $\Gamma^{U-}_{L_1,2}$, a trajectory is generated that, in both forward and reverse time, enters the Jupiter region after one additional perihelion passage, thus modeling the behavior of Oterma in the interior region. To generate a trajectory that additionally enters the Jupiter region in forward time and escapes to the exterior region after $p = 0.5$ revolutions, the perihelion initial conditions, as plotted on the map in gray in fig.(16(a)), that lie within both $\Gamma^{S-}_{L_1,2}$ and $\Gamma^{U-}_{L_1,2}$ are propagated in forward time until entry to the Jupiter region, with the first perijove passage plotted in gray in fig.(16(b)). The first periapses along $W^{U+}_{L_1}$ and $W^{S-}_{L_2,}$ appear in red and blue, respectively, with the region of overlap colored in cyan. The gray perijove points that lie within both $\Gamma^{U+}_{L_1,1}$ and $\Gamma^{S-}_{L_1,1}$ correspond to trajectories that enter the Jupiter region from the interior after three perihelion passages, experience a single passage through perijove, and immediately escape to the exterior region, thus simulating two segments along the path of Oterma. Finally, to enforce that the trajectory additionally enters the Jupiter region in reverse time and escapes to the exterior region after $p = 0.5$ revolutions, the gray perijove points that lie within the cyan region are propagated in reverse time until they re-enter the Jupiter region. The first perijove points upon re-entry appear as gray points within the cyan region in fig.(16(c)), as well as the contours $\Gamma^{S+}_{L_1,1}$ and $\Gamma^{U-}_{L_2,1}$ in blue and red, respectively. Here, cyan represents the region of overlap of these two contours, and it is clear that all of the gray periapses lie inside the cyan region. Thus, propagation of any gray perijove point in figure (16(c)) will produce a trajectory with an itinerary consistent with that of comet Oterma. The selected cometary trajectory approximation appears in blue in fig.(15), and requires 78.93 years of propagation time. This planar path approximation is transitioned into three-dimensions, as described in section (), by enforcing $\rho_p, \theta, \phi, \psi$ constraints on the first periapsis in the Jupiter region. The resulting three-dimensional trajectory appears in fig.(17), and represents an

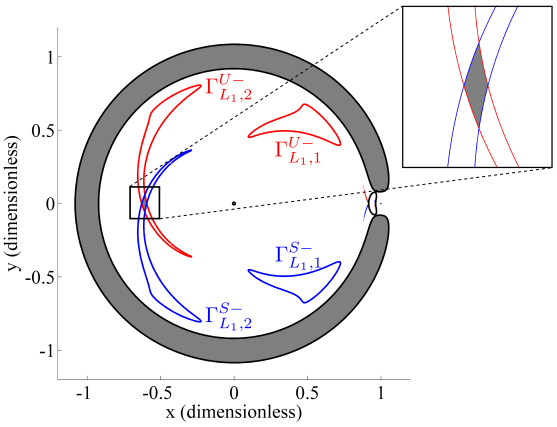

(a) Perihelion map associated with $W^{S-}_{L_1}$ and $W^{U-}_{L_1}$

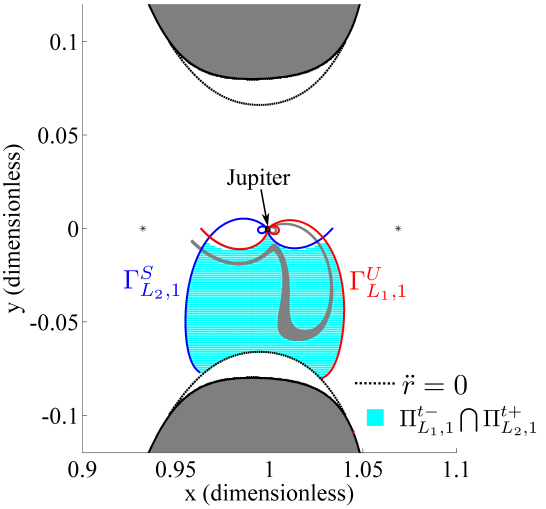

(b) Perijove map associated with $W^{U+}_{L_1}$ and $W^{S-}_{L_2}$ in the Jupiter region

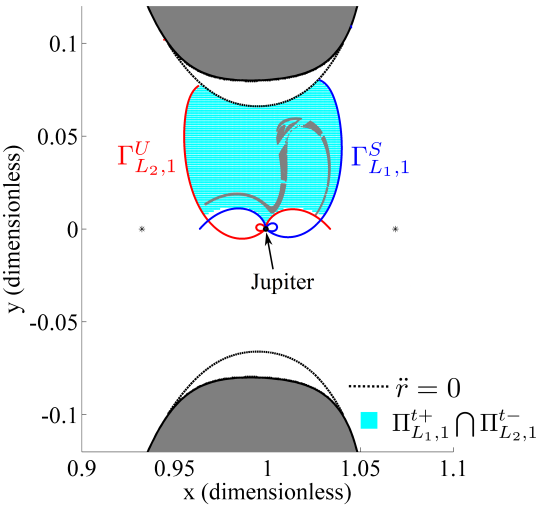

(c) Perijove map associated with $W^{S+}_{L_1}$ and $W^{U-}_{L_2}$ in the Jupiter region

Figure 16. Periapse maps for $C = 3.02$ in the Sun-Jupiter system. (Sun and Jupiter at 10x)

82.14 year propagation.

CONCLUSIONS

The periapse structures within the vicinity of the smaller primary, within the context of the planar CR3BP, prove useful as a design tool for the construction of transit trajectories, as well as heteroclinic connections. Periapse Poincaré maps associated with invariant manifolds allow for the prediction of available solutions for a given system and Jacobi constant value, and are useful in locating solutions with certain desired behaviors in the vicinity of P_2. The techniques developed may be applied to study cometary trajectories in the Sun-Jupiter system. Path approximations are generated for comets Kushida-Muramatsu[1993] and 147P/Oterma, which together represent trajectories possessing both short-term and long-term itineraries, respectively. Within the context of the spatial CR3BP, the periapses associated with three-dimensional escape trajectories are investi-

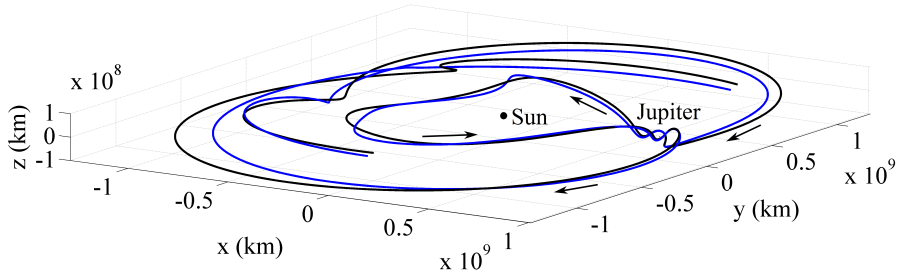

(a) Three-dimensional view

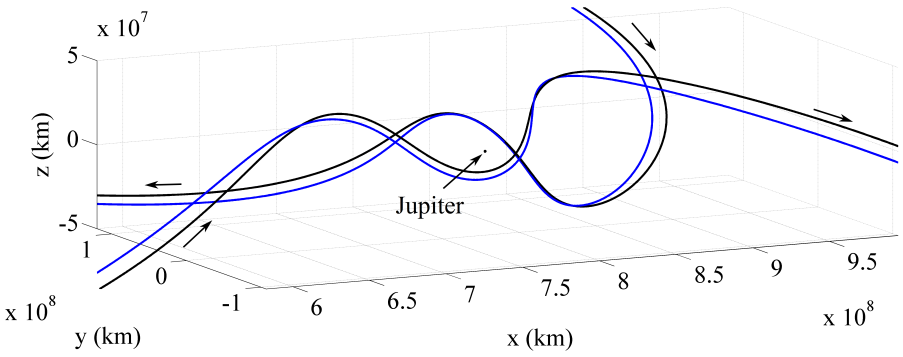

(b) Three-dimensional view near Jupiter

Figure 17. Path of Oterma between 1910 and 1990 (black) and three-dimensional trajectory in CR3BP (blue). (Sun and Jupiter at 20x, $\ell^* = 7.7841202e^8$ km)

gated and a method for locating three-dimensional trajectories possessing pre-determined behaviors is demonstrated by constructing three-dimensional transit trajectories analogous to those computed in the planar problem.

ACKNOWLEDGMENTS

The authors wish to thank the Purdue University Graduate School, the School of Engineering, and the School of Aeronautics and Astronautics for providing funding in support of this work. Special thanks to Ph.D. student Chris Patterson for discussions and insight.

REFERENCES

[1] U. M. Ascher and L. R. Petzold. *Computer Methods for Ordinary Differential Equations and Differential-Algebraic Equations*. Philadelphia, Pennsylvania: Society for Industrial and Applied Mathematics,, 1998.

[2] J. T. Betts. *Practical Methods for Optimal Control Using Nonlinear Programming*. Philadelphia, Pennsylvania: Society for Industrial and Applied Mathematics, 2001.

[3] A. Carusi and G. B. Valsecchi. Temporary Satellite Captures of Comets by Jupiter. *Astronomy and Astrophysics*, 94:226–228, November 1981.

[4] C. C. Conley. Low energy transit orbits in the restricted three-body problem. *Society for Industrial and Applied Mathematics Journal on Applied Mathematics*, 16:732–746, 1968.

[5] G. Gómez, W. S. Koon, M. W. Lo, J. E. Marsden, J. Masdemont, and S. D. Ross. Connecting orbits and invariant manifolds in the spatial restricted three-body problem. *Nonlinearity*, 17:1571–1606, September 2004.

[6] A. F. Haapala. Trajectory design using periapse maps and invariant manifolds. Master's thesis, School of Aeronautics and Astronautics, Purdue University, West Lafayette, Indiana, 2010.

[7] K. C. Howell, B. G. Marchand, and M. W. Lo. Temporary Satellite Capture of Short-Period Jupiter Family Comets from the Perspective of Dynamical Systems. *The Journal of Astronautical Sciences*, 49:539–557, October 2001.

[8] W. S. Koon, M. W. Lo, J. E. Marsden, and S. D. Ross. Heteroclinic connections between periodic orbits and resonance transitions in celestial mechanics. *Chaos*, 10:427–469, June 2000.

[9] B. Marchand. Temporary satellite capture of short period jupiter family comets from the perspective of dynamical systems. Master's thesis, School of Aeronautics and Astronautics, Purdue University, West Lafayette, Indiana, 2000.

[10] K. Ohtsuka, T. Ito, M. Yoshikawa, D. J. Asher, and H. Arakida. Quasi-Hilda comet 147P/Kushida-Muramatsu. Another long temporary satellite capture by Jupiter. *Astronomy and Astrophysics*, 489:1355–1362, October 2008.

[11] M. E. Paskowitz and D. J. Scheeres. Robust Capture and Transfer Trajectories for Planetary Satellite Orbiters. *Journal of Guidance, Control, and Dynamics*, 29:342–353, March 2006.

[12] J. Senent, C. Ocampo, and A. Capella. Low-Thrust Variable-Specific-Impulse Transfers and Guidance to Unstable Periodic Orbits. *Journal of Guidance, Control, and Dynamics*, 28(2):280–290, March 2005.

[13] J. Stoer and R. Bulirsch. *Introduction to Numerical Analysis*. New York: Springer-Verlag, 2002.

[14] B. F. Villac and D. J. Scheeres. Escaping trajectories in the Hill three-body problem and applications. *Journal of Guidance, Control, and Dynamics*, 26:224–232, March 2003.

[15] B. F. Villac and D. J. Scheeres. On The Concept Of Periapsis In Hill's Problem. *Celestial Mechanics and Dynamical Astronomy*, 90:165–178, September 2004.

[16] S. Wiggins, L. Wiesenfeld, C. Jaffé, and T. Uzer. Impenetrable Barriers in Phase-Space. *Physical Review Letters*, 86:5478–5481, June 2001.